IIETA International Information and Engineering Technology Association
Advancing the World of Information and Engineering

Revue des Composites et des Matériaux Avancés-Journal of Composite and Advanced Materials
Vol. 36, No. 2, April, 2026, pp. 219-226
Journal homepage: http://iieta.org/journals/rcma

Modeling and Predicting the Mechanical Properties of Discontinuous Wavy Fiber Composites Based on Contrast and Volume Fraction

Sarra Nacer, Abdennour Benhizia*, Abdelghani Khennab

Structural Mechanics and Materials Laboratory, Department of Mechanical Engineering, Faculty of Technology, University of Batna 2 - Mostefa Ben Boulaïd, Batna 05000, Algeria

Corresponding Author Email: a.benhizia@univ-batna2.dz

https://doi.org/10.18280/rcma.360201

Received: 3 February 2026
Revised: 9 April 2026
Accepted: 20 April 2026
Available online: 30 April 2026

Keywords:
complex microstructure, composite, curve fitting, homogenization, mechanical properties, wavy fiber

ABSTRACT

Discontinuous wavy fibers, originating from natural reinforcements or specific manufacturing processes, exhibit inherent curvature, irregular geometries, and stochastic spatial distributions. These characteristics lead to complex microstructures that significantly influence the mechanical behavior of composite materials. Accurate and efficient prediction of their effective mechanical properties is therefore essential for design and optimization. In this study, finite element-based homogenization is used to evaluate the mechanical behavior of a wavy fiber-reinforced composite. The results are then used to develop analytical models for predicting the effective Young's modulus, shear modulus, and bulk modulus as functions of stiffness contrast and fiber volume fraction. The proposed models show excellent agreement with numerical simulations over a wide range of microstructural configurations, with a coefficient of determination (R^2) exceeding 0.99. By explicitly accounting for the effects of contrast and volume fraction, the developed equations enable fast and robust prediction of effective properties. This provides an efficient framework for the design of composites with complex microstructures.

1. INTRODUCTION

The development of high-performance fiber-reinforced composites has increasingly focused on natural or renewable fibers due to their sustainability, low cost, and favorable mechanical properties. Unlike synthetic straight fibers, many natural or manufactured fibers exhibit wavy morphologies [1], irregular geometries [2], and stochastic spatial distributions [3], which strongly influence the mechanical response of the resulting composites.

Wavy fiber composites can be classified according to fiber orientation, waviness control, morphology, and scale, with each category exhibiting distinct mechanical behavior and processing characteristics. The most common class consists of randomly oriented short wavy fibers, typically produced by injection molding [4] or bulk processing. In these materials, fibers develop three-dimensional curvature due to flow-induced effects and fiber–fiber interactions. Examples include short steel fiber–reinforced thermoplastics, which have been extensively characterized using X-ray micro-computed tomography to reconstruct realistic fiber distributions and mechanical modeling [5].

A second class corresponds to aligned short-wavy fiber composites, in which fibers have a preferred orientation but retain some curvature due to processing or intrinsic fiber morphology [6]. Structures such as partially aligned carbon fiber thermoplastics or natural fiber composites (e.g., flax and hemp) exhibit anisotropic mechanical behavior, including enhanced compressive strength and fatigue resistance. However, fiber waviness may also induce micro-buckling, which locally reduces longitudinal stiffness [7].

Building on these concepts, controlled or engineered wavy fiber composites have been developed using additive manufacturing and architected-design approaches, where fiber curvature is intentionally introduced to improve crack deflection, toughness, and energy absorption. Examples include 3D-printed polymer composites with sinusoidal reinforcement paths and architectured curved fiber patterns [8].

Another emerging category is helical and tortuous fiber composites [9], inspired by biological materials such as bone, tendon, and plant cell walls. In these systems, spiral or helicoidal fiber paths improve damage tolerance, energy absorption, and resilience [10].

Finally, hybrid and multiscale wavy fiber composites combine fibers of different orientations, lengths, or scales, including straight and curved fibers or nanofibers [11]. These architectures are designed to balance stiffness, toughness, and multifunctional properties. Similarly, bio-inspired wavy fiber architectures utilize hierarchical or gradient fiber paths to tailor the local mechanical response and enhance impact resistance [12].

Several studies have demonstrated that fiber waviness is a critical factor governing the mechanical performance of

composite materials. Research in this area can be broadly divided into two categories. The first category reviewed the sources of waviness and their influence on stiffness, strength, and fatigue behavior. In this context, Alves et al. [13] reviewed the sources of waviness and their influence on stiffness, strength, and fatigue behavior, showing that misalignment and out-of-plane curvature reduce the effective stiffness and ultimate strength of composites, as fibers are less efficient at carrying axial loads. In addition, Li et al. [14] investigated delignified bamboo fibers as reinforcement in composites, showing that fiber length, bamboo nodes, and Polyvinyl Alcohol (PVA) treatment significantly affect mechanical performance. They found that long fibers spanning nodes exhibit lower strength due to defects, while PVA treatment enhances fiber–matrix adhesion, highlighting how fiber morphology and microstructural features govern load transfer and composite strength. For compressive strength, Wilhelmsson et al. [15] experimentally demonstrated that in unidirectional non-crimp fabric (NCF) composites, fiber waviness significantly reduces compressive performance, with the extent of reduction depending on the amplitude and wavelength of the misalignment. Similarly, Nishioka et al. [16] analyzed progressive damage around in-plane fiber waviness and showed that even small waviness can significantly reduce tensile and compressive strength.

While these studies provide valuable insight into the origins, characterization, and mechanical consequences of fiber waviness, they predominantly focus on isolated effects under idealized conditions, such as perfectly controlled fiber misalignment or small-scale specimens.

In contrast, the second group of studies has focused on establishing quantitative relationships between microstructural parameters and the effective mechanical properties of fiber composites. Classical micromechanical and semi-empirical models have long been employed to predict the effective properties of discontinuous fiber composites due to their simplicity and low computational cost. Widely used approaches include the Halpin–Tsai formulation, the Mori–Tanaka method, self-consistent models, and rule-of-mixtures–based models. For instance, Tóth and Virág [17] applied modified Halpin–Tsai models incorporating fiber orientation and length correction factors to 3D-printed short fiber composites, achieving errors of approximately 7% in Young's modulus and 18% in tensile strength; however, these models still assume relatively simple, straight fiber geometries and do not account for curvature effects. Similarly, El Dein et al. [18] investigated the reinforcing potential of flax co-products by combining biomass fractionation and microstructural control in thermoplastic composites. Micromechanical models, including the Halpin–Tsai approach, were used to relate composite properties to microstructural parameters. The study highlights the critical role of processing-induced morphology and fiber alignment in maximizing the mechanical performance of sustainable natural fiber composites. In a related study, Ez-Zahraoui et al. [19] proposed a modified Halpin–Tsai model coupled with a self-consistent homogenization scheme to predict the mechanical properties of polypropylene composites reinforced with fly ash and phosphate sludge. Their approach demonstrated that incorporating particle interactions and hybrid reinforcement effects significantly improves prediction accuracy compared with the classical Halpin–Tsai model.

Reviews of micromechanical stiffness predictions confirm that while these models perform well for straight or mildly misaligned fibers, they fail to capture the effects of wavy or curved fibers, including stress redistribution, local bending, and early micro-buckling, because they rely on idealized fiber shapes and empirical orientation factors [20]. In addition, the combined influence of fiber waviness, phase stiffness contrast, soft–hard interactions, fiber volume fraction, and random fiber orientation remains insufficiently represented in current models. This highlights the need for predictive micromechanical frameworks that integrate these parameters to accurately estimate the behavior of wavy fiber composites.

In this study, generalized predictive models for random wavy fiber-reinforced composites are developed by combining finite element-based homogenization with regression-based mathematical modeling. These models explicitly incorporate both fiber–matrix property contrast and fiber volume fraction, enabling accurate and rapid predictions of Young's, shear, and bulk moduli. By integrating high-fidelity simulations with curve-fitting techniques, the models capture the essential relationship between complex microstructural features and macroscopic behavior while significantly reducing computational cost.

2. 3D MICROSTRUCTURE GENERATION

The studied short fiber-reinforced composites are found in applications such as injection-molded polymers and steel, featuring complex microstructures with three-dimensionally oriented, wavy, and occasionally entangled fibers, where fiber waviness naturally arises during processing due to flow, mold geometry, and fiber–fiber interactions (Figure 1(a)). To replicate this in simulations, the composite was modeled in Digimat, where the wavy fibers were represented as non-overlapping curved cylinders having random orientations and distributions (Figure 1(b)), capturing their inherent curvature and spatial variability for accurate prediction of effective mechanical properties.

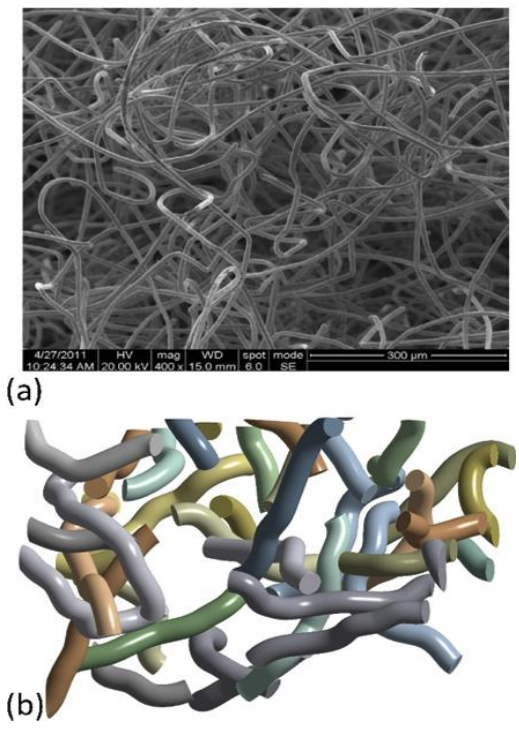

Figure 1. Wavy fibers: (a) SEM image after matrix burn-out [5]; (b) Digimat modeling

The fibers' wavy shape was modeled in Digimat as swept shapes with a circular cross-section and a centerline defined by a random Bézier curve with 11 control points. The first point was fixed, while the remaining points were generated sequentially with random directions and lengths. The fiber waviness is controlled by a tortuosity factor τ that governs the maximum allowable change in orientation between consecutive control points. In this study, a value of $\tau = 10$ was used for fibers with an aspect ratio of 8 to ensure realistic curved fiber geometries.

In Digimat, the representative volume element (RVE) size, number of fibers, and target fiber volume fraction were defined as input parameters, and the software automatically determined the fiber diameter such that the total fiber volume corresponded to the prescribed volume fraction.

An example of a generated RVE containing 200 fibers at a reinforcement volume fraction of 5% is shown in Figure 2.

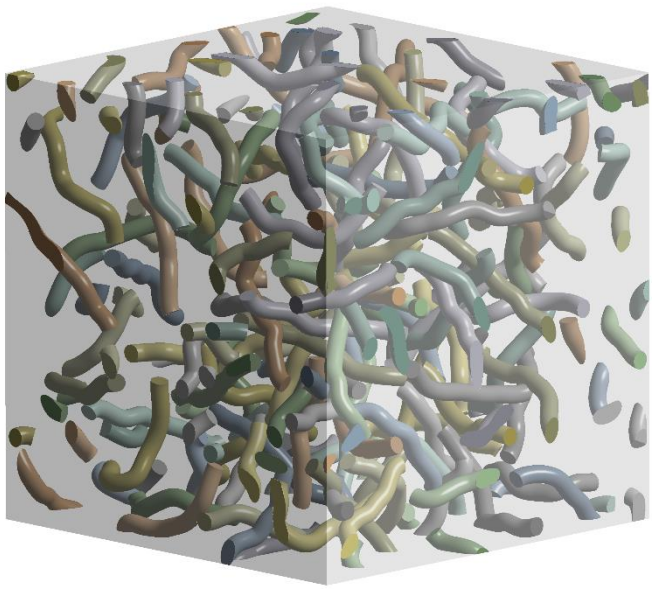

Figure 2. Representative volume element (RVE) of the wavy fiber composite

3. FINITE ELEMENT CALCULATIONS

The effective mechanical properties of the 3D composites, reinforced with curved cylindrical fibers, were estimated using a finite element-based numerical homogenization approach. The simulations were performed using the Zebulon finite element software to accurately evaluate the mechanical response of the resulting composite microstructures.

The analysis focused on two key parameters: contrast C_E and fiber volume fraction. The contrast, defined as the ratio of the reinforcement modulus to that of the matrix, was varied across thirteen values (3, 5, 7, 10, 20, 40, 60, 80, 100, 150, 250, 300, and 350) to systematically explore the effect of hard–soft phase interactions on the overall mechanical response of the composite.

To calculate the contrast C_E between the two phases, the following formula can be used:

$$C_E = \frac{E_f}{E_m} \tag{1}$$

where, E_f and E_m are the Young's moduli of the fibers and the matrix, respectively.

The volume fraction, representing the proportion of reinforcement within the composite, was analyzed at four levels (5%, 10%, 15%, and 20%) to assess the effect of inclusion concentration on the overall mechanical response. The matrix was assigned constant linear elastic properties, with a fixed Young's modulus and Poisson's ratio, as summarized in Table 1.

Table 1. Linear elastic properties of the matrix phase

Elastic Properties	E (Mpa)	ν
Matrix	1000	0.43

Note: E = Young's modulus, ν = Poisson's ratio

3.1 Mesh generation

The 3D composite models were discretized in ANSYS Workbench using fully integrated 10-node quadratic tetrahedral elements (C3D10) to accurately capture stress gradients in complex, curved geometries. The meshed 3D model for a volume fraction of 5% is represented in Figure 3.

The composite mesh was generated with local refinement to ensure adequate resolution of the fiber diameters and fiber–matrix interfaces. A mesh convergence study was conducted, and a mesh size of 0.3 mm, resulting in approximately 300,000 solid elements, was selected as a compromise between accuracy and computational cost.

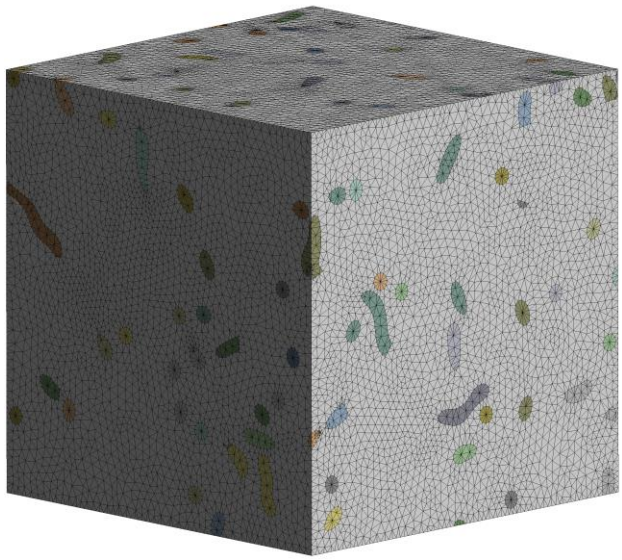

Figure 3. Finite element mesh of the 3D representative volume element (RVE)

3.2 Boundary conditions

The effective mechanical properties of the curved-fiber composite, including Young's modulus, shear modulus, and bulk modulus, were evaluated by applying suitable boundary conditions to the RVE. To reproduce independent macroscopic loading states corresponding to uniaxial tension, pure shear, and hydrostatic compression, separate loading cases were defined. The resulting average stress-strain responses were then used to compute the effective elastic moduli.

- To determine Young's modulus, uniaxial tension was

applied to the 3D RVE by prescribing displacement on one face and constraining the opposite face.

- The bulk modulus K and shear modulus G are determined by applying a macroscopic strain tensor to the boundaries of the RVE, defined as:

$$\underset{\sim}{E_k} = \begin{bmatrix} \frac{1}{3} & 0 & 0 \\ 0 & \frac{1}{3} & 0 \\ 0 & 0 & \frac{1}{3} \end{bmatrix} \quad (2)$$

$$\underset{\sim}{E_\mu} = \begin{bmatrix} 0 & \frac{1}{2} & 0 \\ \frac{1}{2} & 0 & 0 \\ 0 & 0 & 0 \end{bmatrix} \quad (3)$$

The apparent bulk modulus k^{app} and shear modulus μ^{app} were computed from the macroscopic stress–strain responses according to the following relations:

$$k^{app} = \frac{1}{3} trace \langle \underset{\sim}{\sigma} \rangle \quad (4)$$

$$\mu^{app} = \langle \sigma_{12} \rangle \quad (5)$$

where, σ is the local stress tensor, σ_{12} is the local shear tensor component, and < > denotes the average stress over the entire microstructure.

To establish a generalized predictive model for the effective moduli, the results are first characterized individually as functions of contrast and volume fraction. These separate dependencies are then unified into a single formulation to represent their joint contribution to the macroscopic elastic behavior of the composite.

4. RESULTS AND DISCUSSION

4.1 Prediction of effective moduli as a function of contrast

The computed effective moduli, namely Young's modulus, bulk modulus, and shear modulus, were plotted for the four distinct volume fractions across the studied contrast range 3–350 (Figures 4-6) to illustrate the influence of the contrast on the material's elastic behavior. These curves clearly show the evolution of the elastic response as contrast increases.

To quantitatively describe the dependence of the effective elastic moduli on the material contrast, the finite element results were fitted using an optimal analytical curve-fitting function. The proposed equations provide a direct predictive relationship between the homogenized properties, and the contrast parameter is formulated as:

$$E^{eff} = ab^{\frac{1}{C_E}} C_E^{\,c} \quad (6)$$

$$\mu^{eff} = ab^{C_E} C_E^{\,c} \quad (7)$$

$$K^{eff} = \frac{1}{\left(a + bC_E^{\,c}\right)} \quad (8)$$

where, a, b, and c are adjustable coefficients, C_E denotes the contrast variable, and the coefficients are determined by minimizing the fitting error. This approach enables a direct and accurate estimation of the effective moduli as functions of phase contrast, providing a concise mathematical representation of the finite element results.

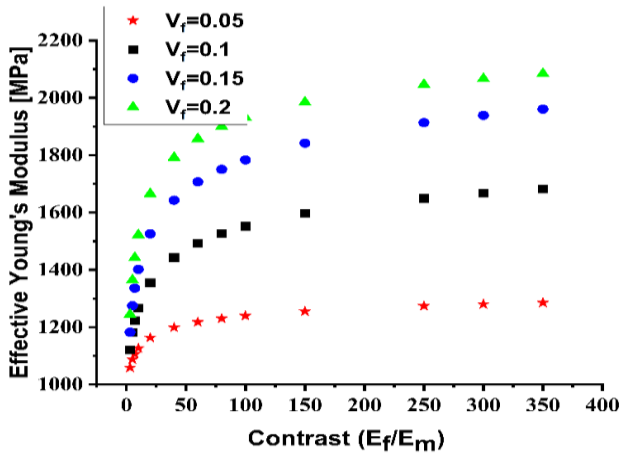

Figure 4. Effective Young's modulus versus contrast for different fiber volume fractions

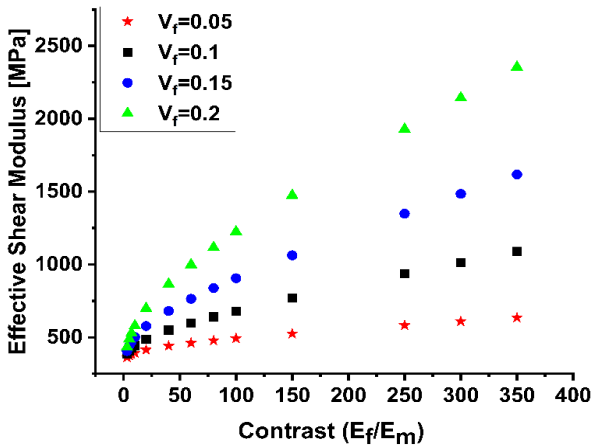

Figure 5. Effective shear modulus versus contrast for different fiber volume fractions

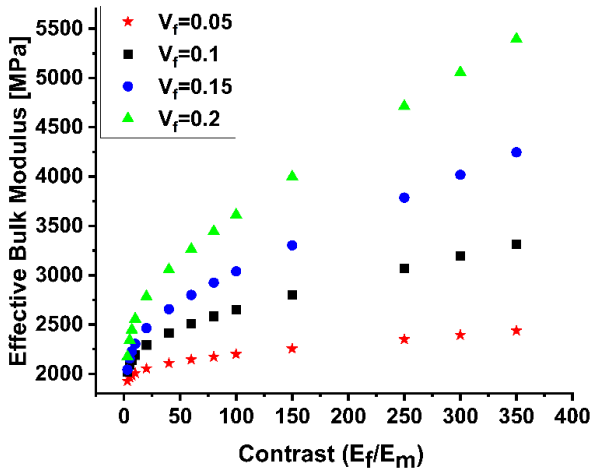

Figure 6. Effective bulk modulus versus contrast for different fiber volume fractions

The optimal fitting coefficients (a, b, and c) identified for each fiber volume fraction and corresponding effective mechanical property are reported in Tables 2-4.

Table 2. Optimal curve-fitting coefficients (a, b, and c) for the effective Young's modulus at different fiber volume fractions

Volume Fraction (%)	*a*	*b*	*c*
5	1059.882	0.881	0.0336
10	1105.4089	0.7977	0.07286
15	1218.9108	0.6681	0.0823
20	1398.625	0.528	0.06976

Table 3. Optimal curve-fitting coefficients (a, b, and c) for the effective shear modulus at different fiber volume fractions

Volume Fraction (%)	*a*	*b*	*c*
5	332	1.0007	0.0698
10	323	1.00124	0.1338
15	314	1.00136	0.1998
20	304.8566	1.001271	0.2745

Table 4. Optimal curve-fitting coefficients (a, b, and c) for the effective bulk modulus at different fiber volume fractions

Volume Fraction (%)	*a*	*b*	*c*
5	0.000552	-0.0000272	0.2798
10	0.00056	-0.00005507	0.26392
15	0.0005989	-0.0000939	0.230624
20	0.00065687	-0.00017622	0.167823

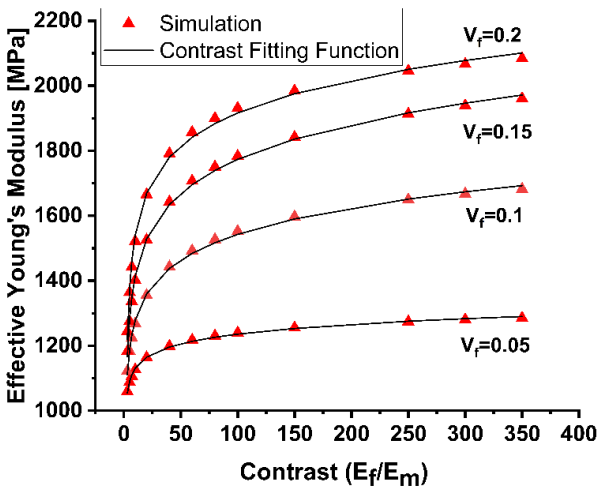

Figure 7. Effective Young's modulus: predicted vs. finite element results as a function of contrast

Figures 7-9 compare the predicted Young's, bulk, and shear moduli from the proposed curve-fitting model with finite element simulation results.

The proposed fitting functions enable direct and accurate prediction of the effective Young's, bulk, and shear moduli as functions of phase contrast, providing a compact mathematical representation of the numerical results. However, a limitation of these functions is that variations in fiber volume fraction require recalibration of the fitting coefficients. Consequently, to extend its applicability, the functions must be generalized to accommodate any desired volume fraction, allowing the prediction of effective moduli across both contrast and volume fraction simultaneously.

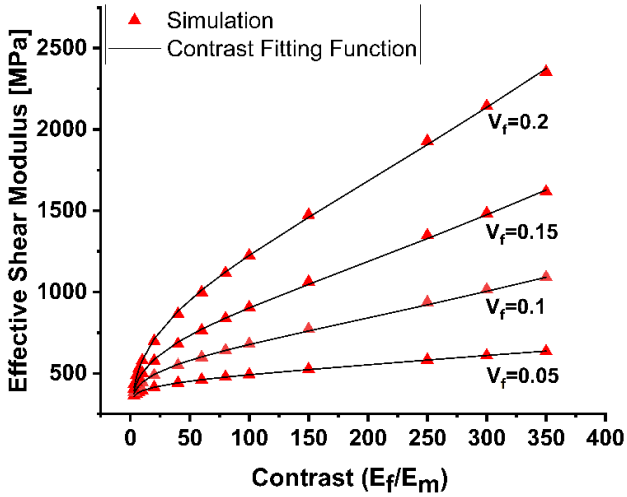

Figure 8. Effective shear modulus: predicted vs finite element results as a function of contrast

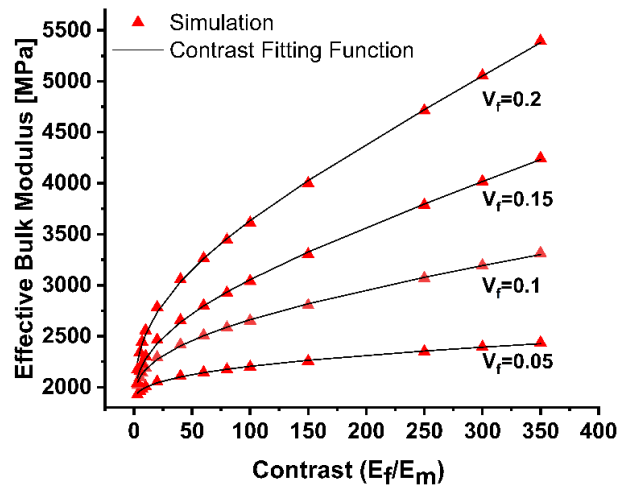

Figure 9. Effective bulk modulus: predicted vs finite element results as a function of contrast

4.2 Generalized moduli prediction based on contrast and volume fraction

To generalize the proposed models across both contrast and fiber volume fractions, the obtained fitting coefficients (a, b, and c) from the contrast-based functions were expressed as functions of the fiber volume fraction. The coefficients were identified separately for each effective modulus.

4.2.1 Young's modulus fitted constants

$$a = a_0 a_1^{V_f} V_f^{a_2} \tag{9}$$

$$b = b_0 b_1^{V_f} V_f^{b_2} \tag{10}$$

$$c = c_0 c_1^{V_f} V_f^{c_2} \tag{11}$$

4.2.2 Shear modulus fitted constants

$$a = a_0 a_1^{V_f} V_f^{a_2} \tag{12}$$

$$b = b_0 b_1^{V_f} V_f^{b_2} \tag{13}$$

$$c = c_0 \left(V_f - c_1\right)^{c_2} \tag{14}$$

4.2.3 Bulk modulus fitted constants

$$a = a_0 a_1^{V_f} V_f^{a_2} \tag{15}$$

$$b = \frac{1}{\left(b_0 + b_1 \ln\left(V_f\right) + b_2 \ln\left(V_f\right)^3\right)} \tag{16}$$

$$c = \frac{c_0}{\left(1 + e^{\left(c_1 - c_2 V_f\right)}\right)} \tag{17}$$

where, a_0, a_1, a_2, b_0, b_1, b_2, c_0, c_1, and c_2 are fitting parameters, their optimized values are summarized in Table 5.

Table 5. Optimal curve-fitting coefficients for Young's, shear, and bulk moduli

Fitting Coefficients	E^{eff}	μ^{eff}	K^{eff}
a_0	446.571	346.758	0.00027407
a_1	49.602	0.5449	17.6294
a_2	-0.2236	0.0042981	-0.18604
b_0	3.2626	1.00583	13118.2418
b_1	0.0016	0.98973	9714.7875
b_2	0.3297	0.001539	765.0472
c_0	79.8879	1.6702	0.2891
c_1	6.97×10^{-8}	-0.019432	-4.4462
c_2	2.3254	1.1928	-20.5602

The integration of all fitted coefficients into a unified formulation governed by fiber volume fraction and contrast leads to the following analytical expressions:

$$E^{eff} = \left(a_0 a_1^{V_f} V_f^{a_2}\right)\left(b_0 b_1^{V_f} V_f^{b_2}\right)^{\left(1/C_E\right)} C_E^{\left(c_0 c_1^{V_f} V_f^{c_2}\right)} \tag{18}$$

$$\mu^{eff} = \left(a_0 a_1^{V_f} V_f^{a_2}\right)\left(b_0 b_1^{V_f} V_f^{b_2}\right)^{C_E} C_E^{c_0\left(V_f - c_1\right)^{c_2}} \tag{19}$$

$$K^{eff} = \frac{1}{\left(\left(a_0 a_1^{V_f} V_f^{a_2}\right) + \left(\frac{1}{\left(b_0 + b_1 \ln\left(V_f\right) + b_2 \ln\left(V_f\right)^3\right)}\right)\right) C_E^{\left(\frac{c_0}{\left(1 + e^{\left(c_1 - c_2 V_f\right)}\right)}\right)}} \tag{20}$$

Figures 10-12 compare the predictions of the unified analytical expressions with the finite element simulation results, showing excellent agreement under all considered conditions. This validation confirms the robustness of the approach. It enables the development of a comprehensive mathematical model capable of accurately predicting the effective Young's, bulk, and shear moduli for any combination of contrast and fiber volume fraction within the studied ranges.

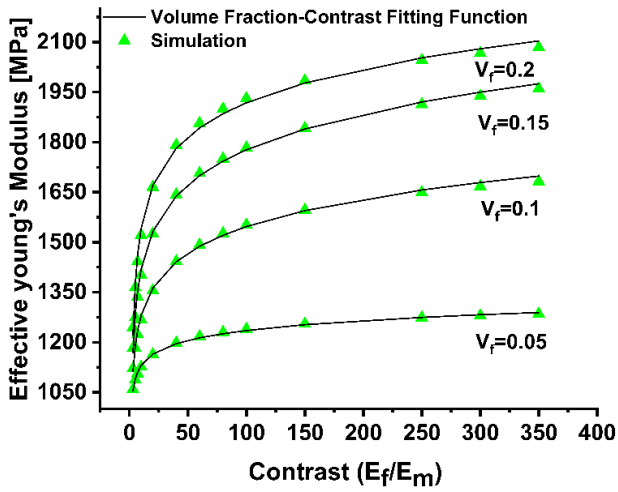

Figure 10. Effective Young's modulus: generalized model predictions vs. finite element results

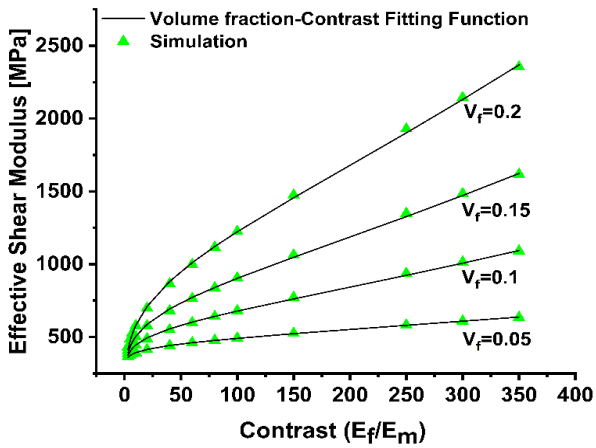

Figure 11. Effective shear modulus: generalized model predictions vs. finite element results

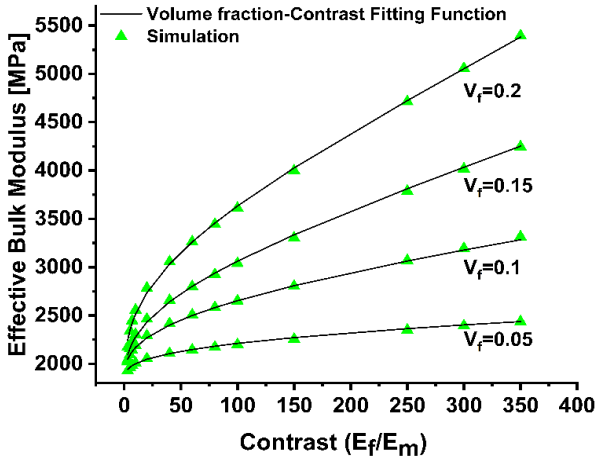

Figure 12. Effective bulk modulus: generalized model predictions vs. finite element results

4.3 Discussion

A detailed analysis of the numerical results provides important insights into the underlying mechanisms governing the mechanical response of curved-fiber composites. The results highlight the coupled influence of stiffness contrast and fiber volume fraction on the effective mechanical behavior of curved-fiber composites. Unlike straight-fiber systems, fiber waviness plays a major role in controlling load transfer efficiency and leads to specific trends observed in the simulations. These results can be explained based on the governing microstructural mechanisms and the interactions between the matrix and reinforcement phases, as outlined below.

4.3.1 Load transfer efficiency and fiber waviness

Fiber waviness reduces reinforcement efficiency because curved fibers initially undergo bending and rotation before carrying axial loads. Part of the applied energy is therefore consumed in fiber straightening, which decreases stiffness compared to straight fibers. This geometric effect explains the lower reinforcement efficiency at low and intermediate contrast values.

4.3.2 Saturation of Young's modulus at high contrast

The saturation of Young's modulus at high stiffness contrast is directly governed by the matrix. Curved or misaligned fibers cannot fully carry axial loads, so deformation is concentrated in the matrix. As a result, further increases in fiber stiffness produce only marginal improvements in the overall modulus.

4.3.3 Spacing between curves and volume fraction

At higher fiber volume fractions, the curves of Young's modulus corresponding to different fractions tend to cluster more closely. This behavior reflects a matrix-dominated response, where the matrix limits the effectiveness of additional reinforcement. As the fiber content increases, the matrix occupies a smaller fraction of the composite but remains the primary phase transmitting deformation, which restricts further increases in stiffness.

4.3.4 Shear and bulk responses

Unlike Young's modulus, the shear and bulk moduli of the composites do not exhibit saturation at high stiffness contrast. The shear response is particularly sensitive to fiber geometry and volume fraction, as curved or misaligned fibers induce localized matrix shear and interfacial stress concentrations. As a result, the shear modulus increases steadily with increasing stiffness contrast, reflecting the continuous enhancement of load transfer through both the fibers and the surrounding matrix.

Similarly, the bulk modulus continues to increase with contrast because volumetric deformation involves contributions from both phases, and the matrix remains able to accommodate additional stress. The absence of saturation indicates that, under shear and volumetric loading, the composite response is less constrained by matrix limitations than under axial loading.

5. CONCLUSION

The effective mechanical behavior of curved-fiber composites was investigated using a finite element-based homogenization approach. The results show that both fiber volume fraction and phase contrast strongly govern the macroscopic elastic response.

A curve-fitting strategy was developed to provide explicit mathematical expressions linking Young's, shear, and bulk moduli to these parameters. While initial formulations were limited to fixed volume fractions, a generalized model was successfully established to enable direct prediction across both contrast and fiber content within the studied ranges.

This framework provides an efficient predictive tool that reduces reliance on computationally expensive simulations and enables rapid estimation of the effective properties of composites with complex wavy fiber architectures.

REFERENCES

[1] Díaz-Montiel, P., Serrato, M., Kohl, M.H., Kohl, J.G. (2026). Effect of ply waviness defects on the viscoelastic properties of carbon/epoxy composites. Composites Part A: Applied Science and Manufacturing, 203: 109575. https://doi.org/10.1016/j.compositesa.2026.109575

[2] Batache, D., Benhizia, A., Khennab, A., Nacer, S. (2024). Influence of platelet boundary irregularity on the nonlinear mechanical behavior of platelet reinforced composites. Revue des Composites et des Matériaux Avancés, 34(1): 1-7. https://doi.org/10.18280/rcma.340101

[3] Seon, G., Makeev, A. (2026). A computer graphics-based method for efficient generation of 3D micromodels of CFRPs and investigation of the effect of random fiber misalignment phase on fiber-direction compressive strength. Composites Science and Technology, 277: 111545. https://doi.org/10.1016/j.compscitech.2026.111545

[4] Fujita, Y., Yeung, W., Kimura, S., Noda, S., Takahashi, J., Greenhalgh, E.S., Pimenta, S. (2026). Predicting failure in injection-moulded short-fibre components through fracture mechanics and fractographic validation. Composite Structures, 381: 120053. https://doi.org/10.1016/j.compstruct.2026.120053

[5] Abdin, Y., Lomov, S.V., Jain, A.K., Lenthe, G.H., Verpoest, I. (2014). Geometrical characterization and micro-structural modeling of short steel fiber composites. Composites Part A: Applied Science and Manufacturing, 67: 171-180. https://doi.org/10.1016/j.compositesa.2014.08.025

[6] Yalaoui, K., Zembouai, I., Kaci, M., Remila, B., Bouzidi, M.A., Bruzaud, S. (2025). Influence of fiber surface modification on morphology and properties of cement/malva fibers composites. Construction and Building Materials, 504: 144646. https://doi.org/10.1016/j.conbuildmat.2025.144646

[7] Lewis, C., Yavuz, B.O., Longana, M.L., Belnoue, J.P.H., Ramakrishnan, K.R., Ward, C., Hamerton, I. (2024). A review on the modelling of aligned discontinuous fibre composites. Journal of Composites Science, 8(8): 318. https://doi.org/10.3390/jcs8080318

[8] Chanraksmey, L., Zhao, W., Han, Y., Chen, Y., Ghita, O., Chen, B. (2025). Recent advances in additive manufacturing of impact-resistant structures with high-performance polymers and their composites. Additive Manufacturing Frontiers, 5(1): 200276. https://doi.org/10.1016/j.amf.2025.200276

[9] Pei, X., Ben, H., Ao, L., Pei, Z. (2026). Investigating twist level control for modulating the impregnation process in high-quality 3D printed continuous flax fiber/PLA composites. Composites Communications, 62: 102726. https://doi.org/10.1016/j.coco.2026.102726
[10] Li, D., Zhu, Z., Zhao, Z., Ji, Y., et al. (2023). Fabrication of helix–fiber composites with mechanically coupled core-wrapping for programmable properties. Communications Materials, 4(1): 28. https://doi.org/10.1038/s43246-023-00355-6
[11] Zhang, X., He, W., Zhao, Z., Yang, M., Li, W. (2026). Micromechanical modeling for the stiffness of nanofiber composites: Synergistic effects of graded interphase, fiber waviness and distribution. Composites Science and Technology, 278: 111583. https://doi.org/10.1016/j.compscitech.2026.111583
[12] Lu, D., Gu, W., Wang, Q., Liao, S., Javed, Z., Mushtaq, M., Wei, Q. (2026). Bioinspired gradient-porous aramid nanofiber aerogel fiber for advanced thermal management. Polymer, 345: 129610. https://doi.org/10.1016/j.polymer.2026.129610
[13] Alves, M.P., Junior, C.C., Ha, S.K. (2021). Fiber waviness and its effect on the mechanical performance of fiber reinforced polymer composites: An enhanced review. Composites Part A: Applied Science and Manufacturing, 149: 106526. https://doi.org/10.1016/j.compositesa.2021.106526
[14] Li, L., Li, H., Chen, Y., Jiang, S., et al. (2025). The potential and challenges of delignified bamboo fiber as reinforcement for composites: The effects of fiber length, bamboo nodes and PVA treatment on strength. Composites Part B: Engineering, 313: 113370. https://doi.org/10.1016/j.compositesb.2025.113370
[15] Wilhelmsson, D., Gutkin, R., Edgren, F., Asp, L.E. (2018). An experimental study of fibre waviness and its effects on compressive properties of unidirectional NCF composites. Composites Part A: Applied Science and Manufacturing, 107: 665-674. https://doi.org/10.1016/j.compositesa.2018.02.013
[16] Nishioka, T., Higuchi, R., Yokozeki, T. (2025). Progressive damage analysis around in-plane fiber waviness in CFRTP laminates under tensile and compressive loading. Composite Structures, 374: 119728. https://doi.org/10.1016/j.compstruct.2025.119728
[17] Tóth, C., Virág, Á.D. (2025). A modified Halpin–Tsai model for the tensile properties of short fiber-reinforced 3D-printed composites using fiber content-dependent orientation correction factor. The International Journal of Advanced Manufacturing Technology, 138(7): 3355-3369. https://doi.org/10.1007/s00170-025-15738-x
[18] El Dein, A.N., Le Moigne, N., Pucci, M.F., Barbulée, A., Gamond, O., Caro, A.S. (2025). Boosting the reinforcing potential of flax co-products: Biomass fractionation and composite microstructure as keys. Industrial Crops and Products, 236: 121925. https://doi.org/10.1016/j.indcrop.2025.121925
[19] Ez-Zahraoui, S., Bouhfid, R., El Achaby, M., Semlali, F.Z. (2025). Mechanical properties prediction of polypropylene composites reinforced with fly ash and/or phosphate sludge using a modified Halpin-Tsai model coupled with a self-consistent approach. Composites Part A: Applied Science and Manufacturing, 202: 109479. https://doi.org/10.1016/j.compositesa.2025.109479
[20] Huang, Z.M., Zhang, C.C., Xue, Y.D. (2019). Stiffness prediction of short fiber reinforced composites. International Journal of Mechanical Sciences, 161: 105068. https://doi.org/10.1016/j.ijmecsci.2019.105068

NOMENCLATURE

E_m	Matrix Young's modulus, MPa
E_f	Fiber Young's modulus, MPa
V_f	Fiber volume fraction, %
C_E	Stiffness contrast
E^{eff}	Effective Young's modulus, MPa
μ^{eff}	Effective shear modulus, MPa
K^{eff}	Effective bulk modulus, MPa
a, b, c	Fitting parameters

Greek symbols

ν	Poisson's ratio
μ^{app}	Effective shear modulus, MPa
k^{app}	Effective bulk modulus, MPa
σ	Local stress tensor, MPa
σ_{12}	Local shear tensor, MPa